# Large-Area and High-Quality 2D Transition Metal Telluride

*Jiadong Zhou, Fucai Liu, Junhao Lin,* Xiangwei Huang, Juan Xia, Bowei Zhang, Qingsheng Zeng, Hong Wang, Chao Zhu, Lin Niu, Xuewen Wang, Wei Fu, Peng Yu, Tay-Rong Chang, Chuang-Han Hsu, Di Wu, Horng-Tay Jeng, Yizhong Huang, Hsin Lin, Zexiang Shen, Changli Yang, Li Lu, Kazu Suenaga, Wu Zhou, Sokrates T. Pantelides, Guangtong Liu,* and Zheng Liu**

Distinct from most semiconducting transition-metal sulfide and selenide compounds that are only stable in the 2H phase, tellurides exhibit much richer structural variations and electronic properties, from semiconducting in the 2H phase to semimetallic in the 1T′ phase. Among all telluride compounds, $MoTe_2$ crystal is stable in both 2H and 1T′ phase while $WTe_2$ only form 1T′ phase in nature (**Figure 1**a). Therefore, transition metal ditellurides, represented by $MoTe_2$ and $WTe_2$, have attracted tremendous interests recently due to the facile switching between different phases and their unique electronic properties. For instance, large and nonsaturating magnetoresistance in $WTe_2$ bulk crystal was reported by Ali et al.,[1] presumably due to the perfect compensation of the electrons and holes even in an ultrahigh magnetic field. A laser-induced transition between 2H and 1T′ phases in $MoTe_2$ thin film has been demonstrated to show an Ohmic homojunction.[2] Furthermore, high mobility up to 4000 and 10 000 $cm^2\ V^{-1}\ s^{-1}$ were reported in $MoTe_2$ and $WTe_2$, respectively.[3,4] $MoTe_2$ and $WTe_2$ atomic layers are also predicted to be promising candidates of type-II Weyl semimetals,[5,6] even in their alloys 1T′ (W, Mo)$Te_2$.[7] More importantly, monolayer tellurides such as $WTe_2$ and $MoTe_2$ are predicted to be 2D topological insulators.[8,9] These make transition metal ditellurides an excellent platform for studying fundamental physical phenomena, such as superconductivity[10] and

J. Zhou, Dr. F. Liu, B. Zhang, Dr. Q. Zeng, Dr. H. Wang, C. Zhu, Dr. L. Niu, X. Wang, Dr. W. Fu, Dr. P. Yu, Prof. Y. Huang, Prof. Z. Shen, Prof. Z. Liu
Centre for Programmable Materials
School of Materials Science and Engineering
Nanyang Technological University
Singapore 639798, Singapore
E-mail: z.liu@ntu.edu.sg

Dr. J. Lin, Prof. W. Zhou, Prof. S. T. Pantelides
Materials Science and Technology Division
Oak Ridge National Lab
Oak Ridge, TN 37831, USA
E-mail: lin.junhao@aist.go.jp

Dr. J. Lin, Prof. S. T. Pantelides
Department of Physics and Astronomy
Vanderbilt University
Nashville, TN 37235, USA

Dr. J. Lin, Prof. K. Suenaga
National Institute of Advanced Industrial Science and Technology (AIST)
Tsukuba 305-8565, Japan

X. Huang, Prof. C. Yang, Prof. L. Lu, Prof. G. Liu
Beijing National Laboratory for Condensed Matter Physics
Institute of Physics
Chinese Academy of Sciences
Beijing 100190, China
E-mail: gtliu@iphy.ac.cn

J. Xia, Prof. Z. Shen
Division of Physics and Applied Physics
School of Physical and Mathematical Sciences
Nanyang Technological University
Singapore 637371, Singapore

Dr. T.-R. Chang, H.-T. Jeng
Department of Physics
National Tsing Hua University
Hsinchu 30013, Taiwan

C.-H. Hsu, D. Wu, Prof. H. Lin
Centre for Advanced 2D Materials and Graphene Research Centre
National University of Singapore
Singapore 117546, Singapore

C.-H. Hsu, D. Wu, Prof. H. Lin
Department of Physics
National University of Singapore
Singapore 117542, Singapore

H.-T. Jeng
Institute of Physics
Academia Sinica
Taipei 11529, Taiwan

Prof. Z. Shen
Centre for Disruptive Photonic Technologies
School of Physical and Mathematical Sciences
Nanyang Technological University
Singapore 637371, Singapore

Prof. C. Yang, Prof. L. Lu
Collaborative Innovation Center of Quantum Matter
Beijing 100871, China

Prof. Z. Liu
Centre for Micro-/Nano-electronics (NOVITAS)
School of Electrical & Electronic Engineering
Nanyang Technological University
50 Nanyang Avenue, Singapore 639798, Singapore

Prof. Z. Liu
CINTRA CNRS/NTU/THALES
UMI 3288
Research Techno Plaza
50 Nanyang Drive, Border X Block, Level 6, Singapore 637553, Singapore

**DOI: 10.1002/adma.201603471**

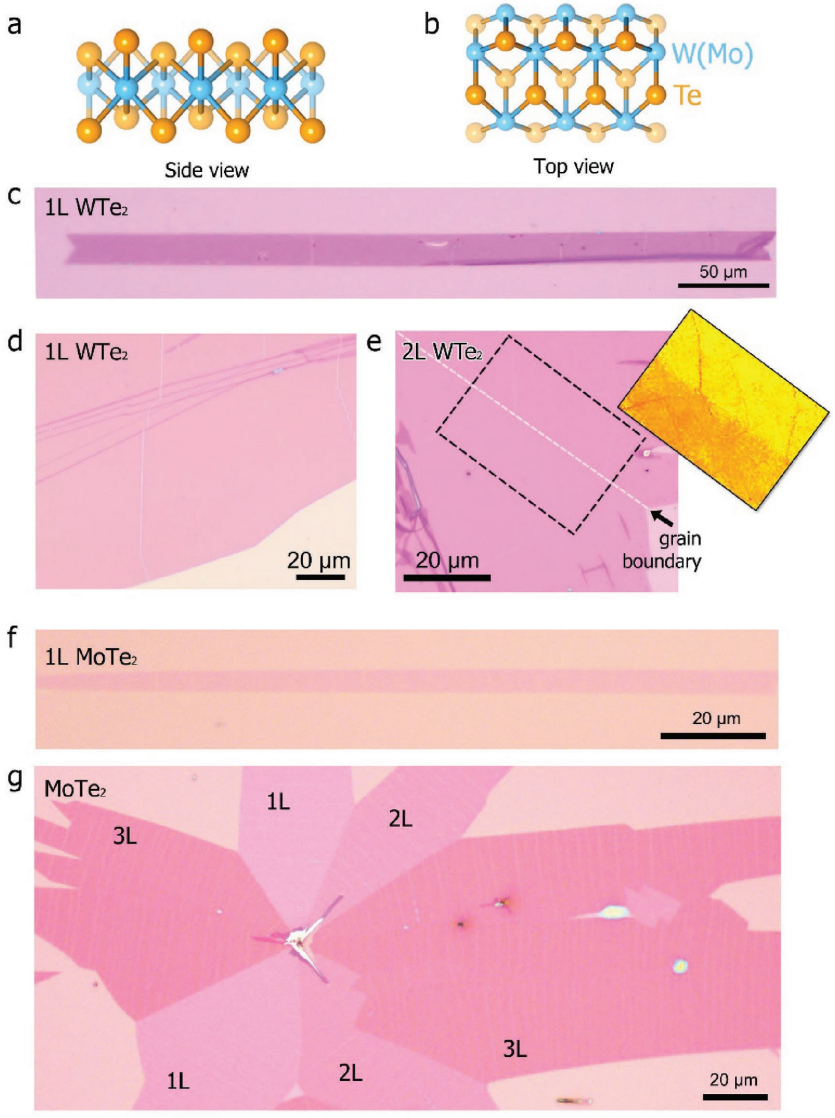


**Figure 1.** Optical geometries of $WTe_2$ and $MoTe_2$ monolayers. a,b) Side and top views of the crystal structure of 1T′ W(Mo)$Te_2$, respectively. c) Optical image of a large single crystalline $WTe_2$ monolayer with a length of ≈350 μm and width of ≈20 μm. d) Optical image of a large $WTe_2$ monolayer film. e) Optical image of a large bilayer $WTe_2$ with grain boundary. The grain boundary is indicated by the arrow and the dashed line. Inset: false color image of the region indicated by the dashed rectangle, highlighting the location of the grain boundary. f) Optical image of a single crystalline $MoTe_2$ monolayer. With the length and width of ≈150 and 8 μm, respectively. g) Optical image of a $MoTe_2$ flake containing 1L, 2L, and 3L $MoTe_2$. The number of layer can be easily identified by their contrast.

quantum spin Hall effect.[8] They are also promising candidates for various potential applications such as spintronics and high-efficiency thermoelectric devices.[11,12]

However, most of the novel physical phenomena in transition-metal ditellurides have been demonstrated in mechanically exfoliated layers, e.g., the magnetoresistance in few-layer $WTe_2$[4] and the superconductivity in bulk 1T′-$MoTe_2$.[13] The exfoliation method is low-yield and time-consuming and only good for scientific research. Direct synthesis of few-layer and monolayer ditelluride would, therefore, be essential to large-scale applications. Among all the growth techniques, chemical vapor deposition (CVD) has been demonstrated as a facile method in synthesizing monolayer crystals in large scale, including graphene,[14] $MoS_2$/$WS_2$,[15,16] $MoSe_2$/$WSe_2$,[17,18] and their heterojunctions,[19–21] by using different precursors under optimized reaction conditions. Although telluride compounds such as $MoTe_2$ films were successfully synthesized by thermal flux and tellurization of molybdenum films,[3,22,23] controlled synthesis of high-quality telluride atomic layers, even down to monolayer, remains elusive under the existing CVD or physical vapor deposition conditions, mainly due to the lower environmental stability and activity of tellurium. For instance, the low chemical reaction activity of W and Mo with Te limits tellurization of W and Mo precursors (powder and oxides), although this method has been widely adopted for the preparation of sulfide and selenide monolayers. More specifically, the electronegativity difference between transitional metal (W or Mo) and Te is very small (≈0.4 or 0.3 eV), indicating a weak bonding between the metals and Te atoms which makes the stoichiometry of ditellurides difficult to be obtained. Furthermore, even though the stoichiometry of $WTe_2$ and $MoTe_2$ is maintained, the as-synthesized product tends to decompose rapidly by emitting Te vapor at high reaction temperature (around 600 °C),[11] instead of evaporating into gas-phase telluride.

Here, we demonstrate a CVD strategy to directly synthesize $WTe_2$ and $MoTe_2$ few-layer and monolayers at large scale. The mixed compounds (weight ratio of the compound metal oxide:metal chlorides:Te is 1:1:1) and Te were used as the source of W (Mo) and Te, respectively. Such configuration of the precursors makes the reaction between Te and the metal sources react easily. The Te in the mixed compounds can decrease the melting point of the mixed compounds, while the other Te powder in the upstream was used as to keep the Te atmosphere in the whole reaction process. The corresponding chemical reaction and more discussion about the role of the mixed compounds are shown in the Supporting Information. Raman spectroscopy was used to characterize the quality of the $WTe_2$ and $MoTe_2$ flakes to confirm their high quality. Two different stacking sequences of $WTe_2$ bilayers were observed by scanning transmission electron microscope (STEM). The as-grown $WTe_2$ atomic layers show nonsaturating magnetoresistance which resembles the features of the mechanical exfoliated ones. A novel semimetal-to-insulator transition is observed in the electrical measurements of $WTe_2$ few layers, whereas the few-layer $MoTe_2$ shows enhanced superconducting behavior.

Side view and top view of the crystal structure of 1T′ $WTe_2$ and $MoTe_2$ are shown in Figure 1a,b, respectively. A schematic diagram of the reaction system is shown in Figure S1(Supporting Information). The reaction temperature is between 750 and 850 °C (see experimental section). The thickness of the $WTe_2$ and $MoTe_2$ atomic layers can be controlled by the growth time. Single crystalline monolayer $WTe_2$ can be consistently obtained in 5 min at 820 °C with specific flow amount of carrier gas (100 sccm Ar/15 sccm $H_2$), while increasing the reaction time results in thick $WTe_2$ flakes. Optical and atomic force microscopy (AFM) images of $WTe_2$ flakes with different thicknesses are shown in Figures S3 and S4 (Supporting Information), respectively. Figure 1c shows a single-crystalline monolayer $WTe_2$ with a length of ≈350 µm and width of ≈20 µm. The sharp edges at the two ends of this rectangle suggest that the edge of $WTe_2$ in 1T′ phase is terminated by planes that are intersected by 50°. Figure 1d shows the optical image of a polycrystalline $WTe_2$ monolayer film with domain size exceeding 100 µm. Figure 1e shows a bilayer $WTe_2$ with a grain boundary at the intersection of two rectangular $WTe_2$ domains (center of the image), as highlighted by the dashed line. For better visibility, the grain boundary with contrast enhancement and false color is shown in the inset of Figure 1e. Furthermore, large-area $WTe_2$ films can be obtained by this method. The corresponding scanning electron microscopy (SEM) images of $WTe_2$ film are shown in Figure S5 (Supporting Information). The size of the $WTe_2$ film is up to 500 µm. Under similar conditions, ribbon-like monolayer 1T′ $MoTe_2$ up to 150 µm (Figure 1f) and few layered 1T′ $MoTe_2$ up to 200 µm (Figure 1g) are also obtained by controlling the Te source according to the phase diagram,[3] indicating that the large-area $MoTe_2$ monolayer film can also be obtained. Unlike $WTe_2$, different number of layers can be found in the same flake, as shown in Figure 1g, where monolayer (1L), bilayer (2L), and trilayer (3L) $MoTe_2$ are clearly distinguished by sharp contrast. AFM and SEM images of $MoTe_2$ flakes are shown in Figures S6 and S7 (Supporting Information), respectively. It is well known that Te-based monolayers are unstable in ambient conditions. The stability test of monolayer $MoTe_2$ and $WTe_2$ are shown in Figure S8 (Supporting Information), which are consistent with the exfoliated ones.

Raman spectroscopy was employed to characterize the quality of the $WTe_2$ and $MoTe_2$ atomic layers. **Figure 2**a shows the Raman spectra of $WTe_2$ films with different thicknesses ranging from monolayer to bulk. For few-layer $WTe_2$ (<10 L), only four optical vibrational modes, namely $B^{10}{}_1$, $A^3{}_2$, $A^7{}_1$, and $A^9{}_1$ were identified, compared with that reported in $WTe_2$ crystal and flakes.[24,25] Interestingly, the $B^{10}{}_1$mode was not reported in few-layer $WTe_2$. Furthermore, the intensity of $A^7{}_1$ peak becomes stronger than other modes as the layer number decreases, similar to the reported result that collected the Raman spectra along *b* axis of the mechanically exfoliated $WTe_2$ atomic layer.[26] These results further confirm the high quality of our as-synthesized $WTe_2$ atomic layers. The optical image and Raman intensity mapping ($A^9{}_1$, ≈205 $cm^{-1}$) of $WTe_2$ is shown in Figure 2b,c, respectively. The region for Raman mapping is highlighted in blue dashed square and the mapping size is around 20 × 20 µm. Raman mapping shows homogeneous intensity across the whole region, which indicates a low defect concentration in the as-synthesized $WTe_2$ monolayers. We also find that the grain boundary in $WTe_2$ can be easily distinguished from the nearby regions in the Raman intensity mapping (Figure S9, Supporting Information). Monolayer and few-layer Raman spectra of $MoTe_2$ are shown in Figure 2d. The Raman peaks in monolayer were observed at 127, 161, 189, and 267 $cm^{-1}$, corresponding to the Raman-active $A_g$ modes of monolayer $MoTe_2$ in 1T′ phase.[27] The spectrum agrees well with the previous reported result.[3,22,28] The Raman spectrum of 2H and 1T′ $MoTe_2$ synthesized by controlling the Te source are shown in Figure S10 (Supporting Information). Figure 2e shows a typical optical image of 1T′ $MoTe_2$ few layers. Raman intensity mapping was collected at the region highlighted by the blue dashed square. Due to the high contrast, monolayer and bilayer $MoTe_2$ can be easily differentiated from Raman mapping (Figure 2f). In addition to Raman characterization, X-ray photoelectron spectroscopy was used to analyze the elemental distribution of $WTe_2$ and $MoTe_2$ atomic layers. The ratio of transition metals (W or Mo) and Te was found to be very close to 1:2, in good agreement with the stoichiometry of $WTe_2$ and $MoTe_2$, as shown in Figure S11 (Supporting Information).

Atom-resolved STEM was applied to further investigate the atomic structure of the as-synthesized $MoTe_2$ and $WTe_2$ atomic layers. **Figure 3**a shows a high-resolution Z-contrast STEM image of a monolayer $WTe_2$, revealing the 1T′ phase which composes of quasi-1D tungsten–tellurium zigzag chains along the *a*-axis of the unit cell (highlighted by the dashed white rectangle) and connected by Te atoms in between, as indicated in the overlaid atomic structural model. The connected Te atoms can also be viewed as a Te chain parallel to the W–Te chains. The fast Fourier transformation (FFT) pattern shown in the inset further confirms the rectangular shape of the $WTe_2$ unit cell. Figure 3b shows a line intensity profile along the *b* axis of the crystal, indicating two distinct positions for Te atoms bonding to the W atom in the distorted 1T phase, with a measured distance of 2.49 and 1.61 Å, respectively. The simulated STEM image using the overlaid atomic structural model achieves a good agreement with the experimental image, as shown in the inset of Figure 3a. We did not observe any intrinsic defects such as vacancies, dislocation, and grain boundaries in all the regions we examined, presumably due to the high reactivity of these defect sites which are easliy oxidized. TEM characterization on thick flakes $WTe_2$ is shown in Figure S12 (Supporting Information), further confirming the high quality of the sample.

The as-synthesized $MoTe_2$ atomic layer also maintains the 1T′ phase similar to the $WTe_2$ in the monolayer form presented above, while structural difference can be observed in the few-layer flakes due to the different interlayer stacking structure, as shown in Figure S13 (Surpporting Information). The electron-energy-loss spectra (EELS) are also provided for direct comparison between the two materials in Figure S13 (Supporting Information). In light of the coexistence of different stacking orders in 2D materials, we also found that the CVD-grown 1T′ $WTe_2$ maintains two different stacking sequences in the bilayer that are similar to other 2D materials. Figure 3c,d shows the atomic structures of two $WTe_2$ bilayer regions, which are distinguishable from each other. Specifically, Figure 3c shows a bilayer stacking where the second layer is mirror symmetric to

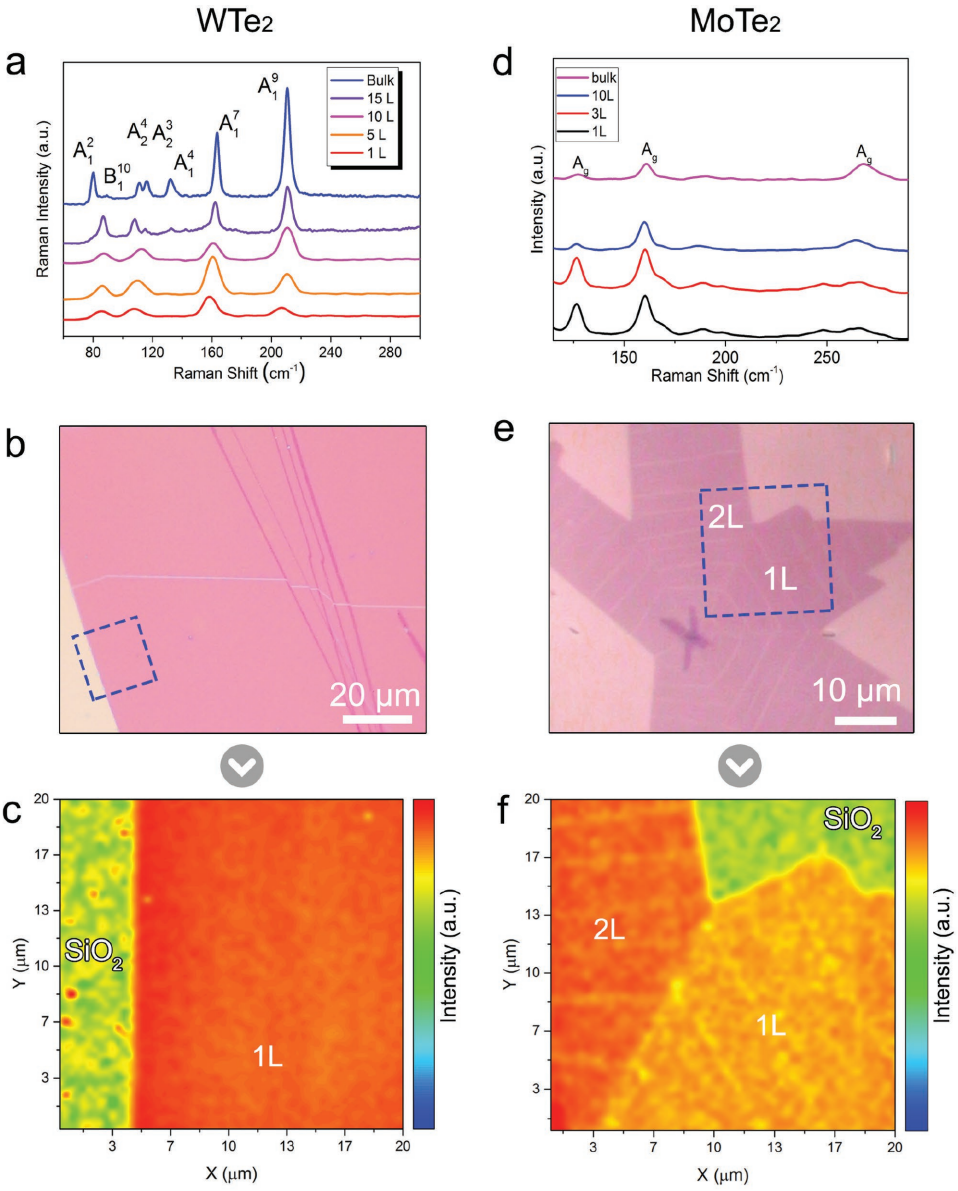


**Figure 2.** Raman spectra and mapping of $WTe_2$ and $MoTe_2$ monolayers. a) Thickness-dependent Raman spectra of $WTe_2$. Seven characteristic vibration modes are identified in bulk $WTe_2$ while only 4 of them can be observed in few-layer $WTe_2$. b) Optical image of a $WTe_2$ monolayer. c) Raman intensity mapping (from $A^9_1$) from the region (highlighted by blue dashed square) in panel (b). The mapping size is $20 \times 20$ μm$^2$. The left side is $SiO_2$ while the right side shows a homogeneous $WTe_2$ film. d) Thickness-dependent Raman spectra of $MoTe_2$. Four characteristic vibration modes are identified in bulk $MoTe_2$. Raman intensity dramatically decreases for all Raman peaks in $MoTe_2$ thin flakes. e) Optical image of $MoTe_2$ containing monolayer and bilayer regions. f) Raman intensity mapping ($A_g$@161 cm$^{-1}$) from the region highlighted by blue dashed square in panel (e). The mapping size is $20 \times 20$ μm$^2$.

the first layer along the *b*-axis of the $WTe_2$ unit cell, as shown by the opposite orientations of the two layers in the top view of the structural model (the dashed diamonds). The Te chains of the second layer align with the W–Te zigzag chains of the first layer vertically, and vice versus, which can be visualized in the side view of the structural model. Such kind of stacking is similar to the 2H stacking in TMDs and AA′ stacking in boron nitride (h-BN). Therefore, we called it 2H stacking following the convention. Figure 3d shows another stacking pattern of $WTe_2$, where the second layer shifts half of a unit cell along the *b* axis away from the 2H stacking shown in Figure 3c, as indicated by the structural model. We called such stacking as 2H′ stacking. Both stackings form periodic stripe patterns, which consist of overlapped Te and W–Te chains from the two layers, in good agreement with the simulated STEM images (Figure S14, Supporting Information). Density functional theory (DFT) calculations on the 2H and 2H′ stacking show very similar band structure, both of which maintain semimetallic properties, as shown in Figure S15 (Surpporting Information). Interlay shifting along *b* axis,[29] however, is rarely observed in $WTe_2$, presumably due to the large interlayer interaction in materials composed by heavy elements. Figure 3e shows an atomically sharp stacking

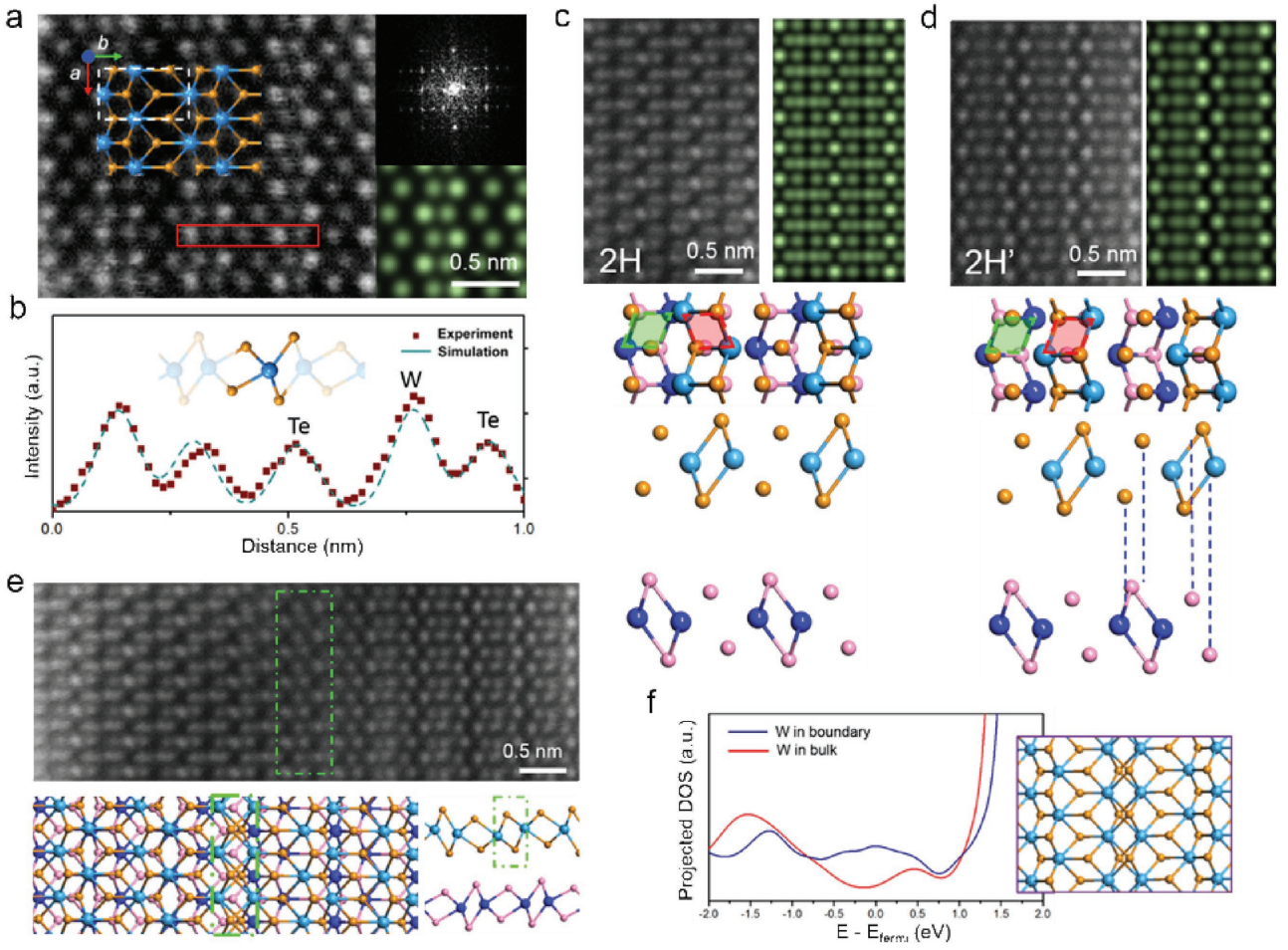


**Figure 3.** Atomic resolution STEM characterization of monolayer and bilayer $WTe_2$. a) STEM Z-contrast image of a monolayer $WTe_2$. The coordinate and structural model are overlaid on the image. Insets: FFT pattern and simulated STEM image of the monolayer $WTe_2$. b) Line intensity profile file of the region highlighted by red rectangle in panel (a). c,d) STEM Z-contrast image of a bilayer $WTe_2$ with c) 2H stacking and d) 2H′ stacking. The green and red dash diamonds indicate the orientation of the zigzag W–Te chains in the first and second layer, respectively. 2H and 2H′ stacking is differed by half of a unit cell shifting along the *b*-aixs in the second layer. Images in green are simulated images. e) STEM Z-contrast image of an atomically sharp stacking boundary between the 2H (left) and 2H′ (right) stacking. The structural model is optimized by DFT calculations. f) Projected DOS of the W atoms in the mirror twin boundary and in the bulk, showing more states near the Fermi level for W atoms in the boundary region. Inset: the structural model of the mirror twin boundary.

boundary between the 2H and 2H′ stacking domains, as highlighted by the green dashed rectangle. A simulated STEM image based on the DFT-relaxed model between the two stackings is shown in Figure S15 (Surpporting Information), which resembles most feature of the stacking boundary observed experimentally. Due to the symmetry of the zigzag chains, the second layers in the two stacking form are also mirror symmetric to each other which forms a mirror twin boundary, similar to the graphene domain wall.[30] DFT calculations further indicate that the $Te_2$ columns are misaligned in the relaxed structure of the mirror twin boundary (inset in Figure 3f), different from those observed in other TMDs.[31–33] A projected density of states (DOS) illustrates (Figure 3f) that the W atoms in the mirror twin boundary show more states at the Fermi level, suggesting that they are more metallic than the bulk counterpart, which may have important contributions in the electrical behavior to the monolayer and few-layer $WTe_2$ and also implications on the quantum spin Hall effect in $WTe_2$.

Layered CVD-grown ditelluride films provide an excellent platform to study the thickness-dependent electric transport. Here, the uniform and large-scaled $WTe_2$ and $MoTe_2$ atomic layers were selected to fabricate devices. The electrical properties of the as-synthesized $WTe_2$ and $MoTe_2$ flakes with different thickness were investigated by means of field- and temperature-dependent transport measurements, as shown in **Figure 4**. Figure 4a shows the resistivity of $WTe_2$ as a function of temperature with thickness of 4 nm (5 layer) and 2 nm (2 layer). The corresponding optical and AFM images of the $WTe_2$ devices are shown in Figure S16 (Surpporting Information). Above 50 K, the resistance of 4 nm $WTe_2$ decreasing monotonically with decreasing temperature shows a metallic behavior, which is similar to the transport properties of the bulk $WTe_2$. However, an upturn in resistance curve was observed with *T* further reduced. Such phenomenon may be due to the 2D electron–electron interactions at the reduced dimension or the degradation of atomically thin $WTe_2$ in air.[34,35] Interestingly, the bilayer $WTe_2$

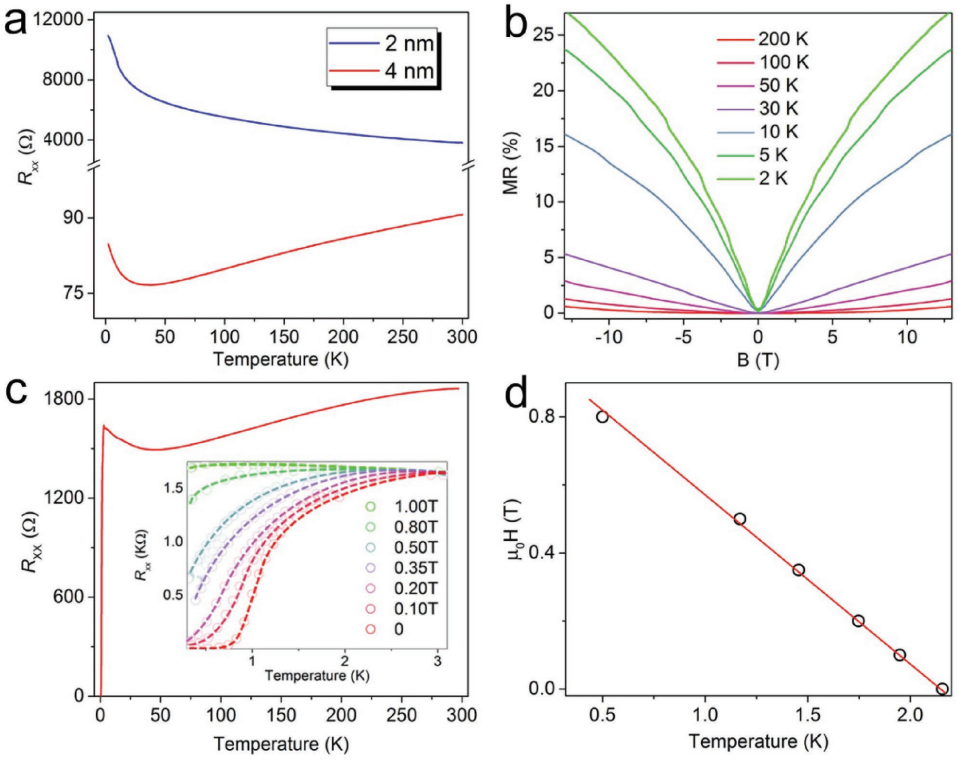


**Figure 4.** Transport in different thicknesses of $WTe_2$ and superconductivity in few layered $MoTe_2$. a) Temperature-dependent resistance of $WTe_2$ flakes with a thickness of 4 and 2 nm under zero magnetic field, respectively. The corresponding field dependent magnetoresistance of 2 nm $WTe_2$ flake at different temperatures is shown in panel (b). $WTe_2$ shows a semimetal-to-insulator transition as the thickness decreased from 4 to 2 nm. c) Superconducting resistive transition of a few layered $MoTe_2$ at zero magnetic field. Inset: Superconductivity of the sample in different perpendicular magnetic fields. d) Temperature dependence of the upper critical field $H_{c2}$. The solid red line is the linear fit to $H_{c2}$.

(with thickness of 2 nm) displays solely insulating behavior under zero magnetic field, confirming that the semimetal-to-insulator transition originates from the effect of the reduced thickness. Such phenomenon has been observed in mechanically exfoliated $WTe_2$ few layers, where the insulating state may be attributed to the Anderson localization in the 2D limit.[4] The temperature-dependent magnetoresistance (MR) calculated by MR = $[\rho(H)-\rho(0)]/\rho(0)$ of bilayer $WTe_2$ as a function of the magnetic field is shown in Figure 4b. These results show that large and nonsaturating magnetoresistance is preserved in our CVD-grown $WTe_2$ even down to a bilayer sample, which further demonstrates their high quality. The MR reaches a maximum value of 28% at 2 K. For the thick $WTe_2$ flakes (12 nm), the MR is about 2000% at 25 K in a field of 10 T, which is shown in Figure S17 (Surpporting Information). These values are close to the order of magnitude of the recent reports.[4]

Enhanced superconductivity is also observed in our as-synthesized few-layer $MoTe_2$. The optical image of the $MoTe_2$ device is shown in Figure S18 (Surpporting Information). Figure 4c shows the longitudinal resistance $R_{xx}$ as a function of temperature $T$ of few-layer $MoTe_2$ device in different perpendicular magnetic fields. $R_{xx}$ decreases steadily from 300 to 40 K, indicating that the sample shows a metallic behavior which is consistent with previous studies on exfoliated samples.[3] With $T$ further reduced, the sample gradually becomes superconducting below $T$ = 2.5 K (the onset of transition) and reaches zero resistance at $T_c$ = 0.5 K. Surprisingly, the superconductivity in thinner samples is strongly enhanced compared with $T_c$ = 0.1 K reported in its bulk counterpart.[13] The possible reason may be an enhancement of the effective electron–phonon coupling constant in thinner samples.[36] The inset of Figure 4c displays the longitudinal resistance $R_{xx}$ as a function of temperature in different perpendicular magnetic fields. We define the superconducting transition temperature $T_c$ under different magnetic fields as the temperature at which the resistance drops to 10% of the normal state resistance $R_N$. $T_c$ shifts systematically to lower temperatures with increasing magnetic fields $B$. Finally, the superconductivity was completely suppressed when $B \geq 1$ T. We summarize the upper critical field $H_{c2}$-$T_c$ phase diagram in Figure 4d and find a linear relationship between $H_{c2}$ and $T_c$ near $T_c$. This is a characteristic of 2D superconductors and can be explained by the standard linearized Ginzburg–Landau (GL) theory

$$H_{c2}(T) = \frac{\phi_0}{2\pi\xi_{GL}(0)^2}\left(1-\frac{T}{T_c}\right) \quad (1)$$

where $\xi_{GL}$ (0) is the zero-temperature GL in-plane coherence length and $\phi_0$ is the magnetic flux quantum. By fitting the experimental data with the above formula, a coherence length of 38 nm was obtained, which is much larger than that in $Mo_2C$.[37]

In summary, large-scale and atom-thin ditellurides including $WTe_2$ and $MoTe_2$ were synthesized. Complementary

characterizations demonstrated the high-quality of as-grown samples. High-resolution STEM imaging resolved the atomic structure of $WTe_2$ and $MoTe_2$ and also observed the domain wall in bilayer $WTe_2$ where the stacking boundary are revealed between two distinct stacking sequences. Electric transport measurement also revealed the semimetal-to-insulator transition in $WTe_2$ and enhanced superconductivity in $MoTe_2$. Our work will shed light on the synthesis of atom-thin telluride materials and boost the realization of quantum spin Hall devices.

## Experimental Section

*Synthesis of $MoTe_2$ and $WTe_2$*: The $WTe_2$ ($MoTe_2$) crystals were synthesized by CVD method using $WO_3$ ($MoO_3$) and $WCl_6$ ($MoCl_5$) (Sigma) as the W sources. The Te powder was used as the Te sources. The crystals were synthesized in quartz tube (1 in. diameter) with temperature from 700 to 850 °C. The system of the reaction is shown in Figure S1(Supporting Information). Specifically, for the $WTe_2$, the mixed gas of $H_2$/Ar with 15 and 150 sccm was used as the carrier gas, the silicon boat containing 30 mg mixed powders with $WO_3$:$WCl_6$:Te = 1:1:1(weight ratio) was put in the center of the tube. The $SiO_2$/Si substrate was placed downstream. Another silicon boat containing 0.5 g Te powder was put on the upstream. The temperature ramps up to the 820 °C in 17 min, and keeping at the reaction temperature for about 5 to 15 min. Then, the furnace cools down to room temperature gradually. For the $MoTe_2$, the mixed gas of $H_2$/Ar with 15 and 200 sccm was used as the carrier gas, the silicon boat containing 30 mg mixed powder with $MoO_3$:$MoCl_5$:Te = 1:1:1 was put in the center of the tube. The $SiO_2$/Si substrate was placed downstream. Another silicon boat containing 0.5 g Te powders was put on the upstream. The temperature ramped up to the 780 °C in 16 min, and kept at the reaction temperature for about 5 to 15 min. Then, the furnace cooled down to room temperature gradually. Detailed description of the growth is given in the Supporting Information.

*Raman Characterization*: Raman measurements with an excitation laser of 532 nm were performed using a WITEC alpha 200R Confocal Raman system. Before Raman characterization, the system was calibrated with the Raman peak of Si at 520 $cm^{-1}$. The laser powers are less than 1 mW to avoid overheating of the samples.

*TEM and STEM Characterization*: The STEM samples were prepared with a poly(methyl methacrylate) (PMMA) assisted method. A layer of PMMA of about 1 µm thick was spin-coated on the wafer with $WTe_2$ ($MoTe_2$) samples deposited, and then baked at 180 °C for 3 min. Afterward, the wafer was immersed in NaOH solution (1 M) to etch the $SiO_2$ layer overnight. After lift-off, the PMMA/$WTe_2$ ($MoTe_2$) film was transferred into DI water for several cycles to wash away the residual contaminants, and then it was fished by a TEM grid (Quantifoil Mo grid). The transferred specimen was dried naturally in ambient environment, and then dropped into acetone overnight to wash away the PMMA coating layers. The STEM imaging shown in the main text was performed on an aberration-corrected Nion UltraSTEM-100 operating at 100 kV. The convergence semiangle for the incident probe was 31 mrad. Z-contrast images were collected for a half-angle range of ≈86–200 mrad. STEM imaging and EELS analysis on $MoTe_2$ shown in the Supporting Information were performed on a JEOL 2100F with a cold field-emission gun and an aberration corrector (the DELTA-corrector) operating at 60 kV. A Gatan GIF Quantum was used for recording the EELS spectra. The inner and outer collection angles for the STEM image ($\beta$1 and $\beta$2) were 62 and 129–140 mrad, respectively, with a convergence semiangle of 35 mrad. The beam current was about 15 pA for the ADF imaging and EELS chemical analyses. All imaging was performed at room temperature.

*Devices Fabrication and Transport Measurement*: The Hall bars were patterned on few layer $MoTe_2$ and $WTe_2$ using e-beam lithography. The Ti/Au (5/50 nm) electrodes were deposited using the thermal evaporator, followed by the lift off process. For the measurements of $WTe_2$, the transport measurement was performed in the Quantum Design PPMS system with temperature ranging from 300 to 2 K and magnetic field up to 14 T. For the superconductivity measurements of $MoTe_2$, the transport experiment was carried out in a top-loading Helium-3 cryostat in a superconducting magnet. An AC probe current $I_{AC}$ = 10 nA at 30.9 Hz was applied from the source to the drain. Then, a lock-in amplifier monitored the longitudinal $R_{xx}$ through two additional electrical contacts.

## Supporting Information

Supporting Information is available from the Wiley Online Library or from the author.

## Acknowledgements

J.Z., F.L., J.L., and X.H. contributed equally to this work. This work was supported by the Singapore National Research Foundation under NRF RF Award No. NRF-RF2013-08, the start-up funding from Nanyang Technological University (M4081137.070 ), and supported from the Ministry of Education Singapore under grant No. MOE2015-T2-2-007 and RG164/15. J.L. and K.S. acknowledge support from the JST Research Acceleration Programme. This research was also supported in part by U.S. DOE grant DE-FG02-09ER46554 (J.L. and S.T.P.), by the U.S. Department of Energy, Office of Science, Basic Energy Science, Materials Sciences and Engineering Division (W.Z.), and through a user project at ORNL's Center for Nanophase Materials Sciences (CNMS), which is a DOE Office of Science User Facility. This research used resources of the National Energy Research Scientific Computing Center, which was supported by the Office of Science of the US Department of Energy under Contract No. DE-AC02-05CH11231. T.-R.C. and H.-T.J. were supported by the Ministry of Science and Technology, National Tsing Hua University, and Academia Sinica, Taiwan. The authors also thank NCHC, CINC-NTU, and NCTS, Taiwan for technical support. H.L. acknowledges the Singapore National Research Foundation for the support under NRF Award No. NRF-NRFF2013-03. The work at IOP was supported by the National Basic Research Program of China from the MOST under the Grant Nos. 2014CB920904 and 2013CB921702, by the NSFC under the Grant Nos. 11174340 and 91421303.

Received: July 1, 2016
Revised: September 19, 2016
Published online: November 17, 2016

[1] M. N. Ali, J. Xiong, S. Flynn, J. Tao, Q. D. Gibson, L. M. Schoop, T. Liang, N. Haldolaarachchige, M. Hirschberger, N. P. Ong, R. J. Cava, *Nature* **2014**, *514*, 205.
[2] S. Cho, S. Kim, J. H. Kim, J. Zhao, J. Seok, D. H. Keum, J. Baik, D. H. Choe, K. J. Chang, K. Suenaga, S. W. Kim, Y. H. Lee, H. Yang, *Science* **2015**, *349*, 625.
[3] D. H. Keum, S. Cho, J. H. Kim, D. H. Choe, H. J. Sung, M. Kan, H. Kang, J. Y. Hwang, S. W. Kim, H. Yang, K. J. Chang, Y. H. Lee, *Nat. Phys.* **2015**, *11*, 482.
[4] L. Wang, I. Gutierrez-Lezama, C. Barreteau, N. Ubrig, E. Giannini, A. F. Morpurgo, *Nat. Commun.* **2015**, *6*, 8892.
[5] A. A. Soluyanov, D. Gresch, Z. J. Wang, Q. S. Wu, M. Troyer, X. Dai, B. A. Bernevig, *Nature* **2015**, *527*, 495.
[6] Y. Sun, S. C. Wu, M. N. Ali, C. Felser, B. H. Yan, *Phys. Rev. B* **2015**, *92*, 161107.
[7] T. R. Chang, S. Y. Xu, G. Chang, C. C. Lee, S. M. Huang, B. Wang, G. Bian, H. Zheng, D. S. Sanchez, I. Belopolski, N. Alidoust,

M. Neupane, A. Bansil, H. T. Jeng, H. Lin, M. Z. Hasan, *Nat. Commun.* **2016**, *7*, 10639.
[8] X. F. Qian, J. W. Liu, L. Fu, J. Li, *Science* **2014**, *346*, 1344.
[9] A. A. Lukas Muechler, T. Neupert, R. Car, **2016**, *arXiv*: *1604*. 01398.
[10] D. F. Kang, Y. Z. Zhou, W. Yi, C. L. Yang, J. Guo, Y. G. Shi, S. Zhang, Z. Wang, C. Zhang, S. Jiang, A. G. Li, K. Yang, Q. Wu, G. M. Zhang, L. L. Sun, Z. X. Zhao, *Nat. Commun.* **2015**, *6*, 7804.
[11] J. E. Callanan, G. A. Hope, R. D. Weir, E. F. Westrum, *J. Chem. Thermodyn.* **1992**, *24*, 627.
[12] P. A. G. Ohare, G. A. Hope, *J. Chem. Thermodyn.* **1992**, *24*, 639.
[13] Y. P. Qi, P. G. Naumov, M. N. Ali, C. R. Rajamathi, W. Schnelle, O. Barkalov, M. Hanfland, S. C. Wu, C. Shekhar, Y. Sun, V. Suss, M. Schmidt, U. Schwarz, E. Pippel, P. Werner, R. Hillebrand, T. Forster, E. Kampert, S. Parkin, R. J. Cava, C. Felser, B. H. Yan, S. A. Medvedev, *Nat. Commun.* **2016**, *7*, 11038.
[14] T. R. Wu, X. F. Zhang, Q. H. Yuan, J. C. Xue, G. Y. Lu, Z. H. Liu, H. S. Wang, H. M. Wang, F. Ding, Q. K. Yu, X. M. Xie, M. H. Jiang, *Nat. Mater.* **2016**, *15*, 43.
[15] Y. Gao, Z. B. Liu, D. M. Sun, L. Huang, L. P. Ma, L. C. Yin, T. Ma, Z. Y. Zhang, X. L. Ma, L. M. Peng, H. M. Cheng, W. C. Ren, *Nat. Commun.* **2015**, *6*, 8569.
[16] S. Najmaei, Z. Liu, W. Zhou, X. L. Zou, G. Shi, S. D. Lei, B. I. Yakobson, J. C. Idrobo, P. M. Ajayan, J. Lou, *Nat. Mater.* **2013**, *12*, 754.
[17] J. K. Huang, J. Pu, C. L. Hsu, M. H. Chiu, Z. Y. Juang, Y. H. Chang, W. H. Chang, Y. Iwasa, T. Takenobu, L. J. Li, *ACS Nano* **2014**, *8*, 923.
[18] X. L. Wang, Y. J. Gong, G. Shi, W. L. Chow, K. Keyshar, G. L. Ye, R. Vajtai, J. Lou, Z. Liu, E. Ringe, B. K. Tay, P. M. Ajayan, *ACS Nano* **2014**, *8*, 5125.
[19] Y. J. Gong, J. H. Lin, X. L. Wang, G. Shi, S. D. Lei, Z. Lin, X. L. Zou, G. L. Ye, R. Vajtai, B. I. Yakobson, H. Terrones, M. Terrones, B. K. Tay, J. Lou, S. T. Pantelides, Z. Liu, W. Zhou, P. M. Ajayan, *Nat. Mater.* **2014**, *13*, 1135.
[20] C. M. Huang, S. F. Wu, A. M. Sanchez, J. J. P. Peters, R. Beanland, J. S. Ross, P. Rivera, W. Yao, D. H. Cobden, X. D. Xu, *Nat. Mater.* **2014**, *13*, 1096.
[21] M. Y. Li, Y. M. Shi, C. C. Cheng, L. S. Lu, Y. C. Lin, H. L. Tang, M. L. Tsai, C. W. Chu, K. H. Wei, J. H. He, W. H. Chang, K. Suenaga, L. J. Li, *Science* **2015**, *349*, 524.
[22] J. C. Park, S. J. Yun, H. Kim, J. H. Park, S. H. Chae, S. J. An, J. G. Kim, S. M. Kim, K. K. Kim, Y. H. Lee, *ACS Nano* **2015**, *9*, 6548.
[23] C. H. Naylor, W. M. Parkin, J. L. Ping, Z. L. Gao, Y. R. Zhou, Y. Kim, F. Streller, R. W. Carpick, A. M. Rappe, M. Drndic, J. M. Kikkawa, A. T. C. Johnson, *Nano Lett.* **2016**, *16*, 4297.
[24] M. K. Jana, A. Singh, D. J. Late, C. R. Rajamathi, K. Biswas, C. Felser, U. V. Waghmare, C. N. R. Rao, *J. Phys. Condens. Matter* **2015**, *27*, 285401.
[25] Y. Kim, Y. I. Jhon, J. Park, J. H. Kim, S. Lee, Y. M. Jhon, *Nanoscale* **2016**, *8*, 2309.
[26] Y. C. Jiang, J. Gao, L. Wang, *Sci. Rep.-UK* **2016**, *6*, 19624.
[27] M. Kan, H. G. Nam, Y. H. Lee, Q. Sun, *Phys. Chem. Chem. Phys.* **2015**, *17*, 14866.
[28] L. Zhou, K. Xu, A. Zubair, A. D. Liao, W. J. Fang, F. P. Ouyang, Y. H. Lee, K. Ueno, R. Saito, T. Palacios, J. Kong, M. S. Dresselhaus, *J. Am. Chem. Soc.* **2015**, *137*, 11892.
[29] X. Lu, M. I. B. Utama, J. H. Lin, X. Luo, Y. Y. Zhao, J. Zhang, S. T. Pantelides, W. Zhou, S. Y. Quek, Q. H. Xiong, *Adv. Mater.* **2015**, *27*, 4502.
[30] L. Brown, R. Hovden, P. Huang, M. Wojcik, D. A. Muller, J. Park, *Nano Lett.* **2012**, *12*, 1609.
[31] X. Lu, M. I. B. Utama, J. H. Lin, X. Gong, J. Zhang, Y. Y. Zhao, S. T. Pantelides, J. X. Wang, Z. L. Dong, Z. Liu, W. Zhou, Q. H. Xiong, *Nano Lett.* **2014**, *14*, 2419.
[32] A. M. van der Zande, P. Y. Huang, D. A. Chenet, T. C. Berkelbach, Y. M. You, G. H. Lee, T. F. Heinz, D. R. Reichman, D. A. Muller, J. C. Hone, *Nat. Mater.* **2013**, *12*, 554.
[33] J. H. Lin, S. T. Pantelides, W. Zhou, *ACS Nano* **2015**, *9*, 5189.
[34] J. Hu, X. Liu, C. L. Yue, J. Y. Liu, H. W. Zhu, J. B. He, J. Wei, Z. Q. Mao, L. Y. Antipina, Z. I. Popov, P. B. Sorokin, T. J. Liu, P. W. Adams, S. M. A. Radmanesh, L. Spinu, H. Ji, D. Natelson, *Nat. Phys.* **2015**, *11*, 471.
[35] W. L. Liu, **2016**, *arXiv*: *1608*. 04801.
[36] E. Navarro-Moratalla, J. O. Island, S. Manas-Valero, E. Pinilla-Cienfuegos, A. Castellanos-Gomez, J. Quereda, G. Rubio-Bollinger, L. Chirolli, J. A. Silva-Guillen, N. Agrait, G. A. Steele, F. Guinea, H. S. J. van der Zant, E. Coronado, *Nat. Commun.* **2016**, *7*, 11043.
[37] C. Xu, L. B. Wang, Z. B. Liu, L. Chen, J. K. Guo, N. Kang, X. L. Ma, H. M. Cheng, W. C. Ren, *Nat. Mater.* **2015**, *14*, 1135.